Journal of Membrane Science & Research

journal homepage: www.msrjournal.com

Research Paper

Quinary-Phase-Field Simulation and Parametric Investigation of Modified PVDF Membrane Morphogenesis

Cao Rong Fei, Ping Fang *, Wang Qi, Zhang Zhuo, Sun Yu Jiao

Xi'an Polytechnic University No. 58, Shangu Avenue, Lintong District, Xi'an, Shaanxi Province, 710600, China

Article info

Received 2025-09-17
Revised 2025-11-14
Accepted 2025-11-15
Available online 2025-11-15

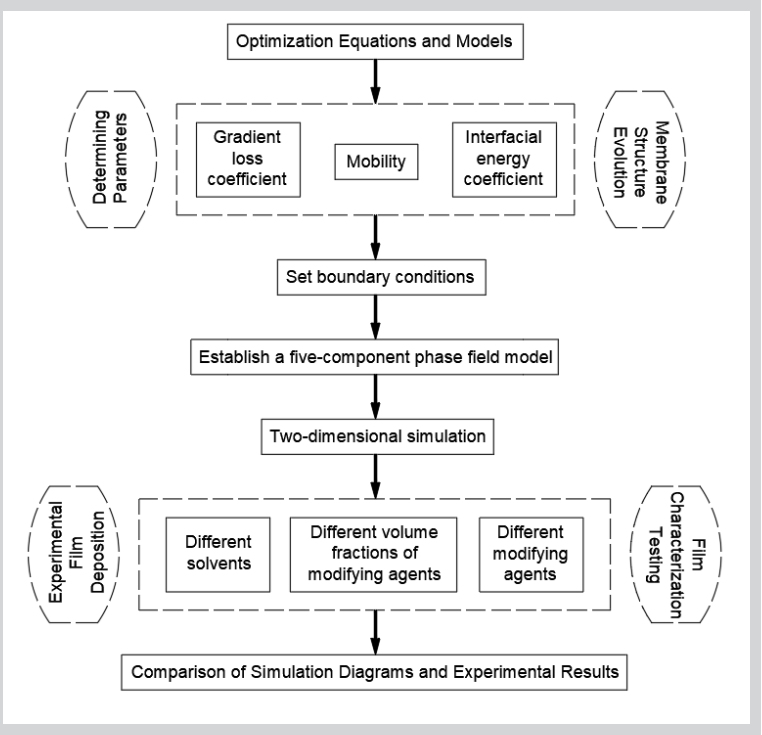
Keywords

Non-solvent induced phase transition (NIPS)
Quinary phase-field model
Modified PVDF membrane
Mechanism analysis
Model parameters

Highlights

- First builds five-component phase-field model for PVDF system using Cahn-Hilliard equation and Flory-Huggins theory.
- Solvent type (TEP/DMF/DMAc) adjusts phase separation rate, notably affecting PVDF membrane pore structure and performance.
- GO (0.4%) optimizes pore distribution; TiO_2 (3.5%) promotes PVDF β-phase, both boosting membrane performance.
- Model (deviation <5% from experiments) serves as quantitative tool for multi-parameter optimization of high-performance PVDF membranes.

Graphical abstract



Abstract

Current research on PVDF membrane preparation is predominantly experimental, which limits a thorough understanding of the microscopic film-forming mechanisms. Moreover, the synergistic effects of solvents and modifiers on phase separation kinetics have not been systematically integrated into multicomponent analyses, impeding the precise design of high-performance membranes. To address this, we developed a phase-field model for the PVDF/DMAc/H_2O/PVP/modifier quinary system based on the Cahn-Hilliard equation and Flory-Huggins theory. This model, for the first time, incorporates solvent-modifier synergy into the kinetic analysis of multicomponent phase separation to simulate the immersion precipitation process. Our results demonstrate that solvent type critically influences membrane pore structure by regulating phase separation rates (e.g., instantaneous for TEP versus delayed for DMF). Among the modifiers, graphene oxide (GO) at 0.4% vol. optimized molecular arrangement, yielding a uniform pore distribution with a water flux of 895.64 $L/m^2 \cdot h^{-1}$ and a rejection rate of 87.35%. Titanium dioxide (TiO_2) at 3.5% vol. exhibited superior overall performance by promoting the PVDF β-phase transformation. The model elucidates underlying micro-mechanisms through thermodynamic-kinetic coupling, showing less than 5% deviation from experimental data, thereby providing a quantitative tool for the multi-parameter synergistic optimization of high-performance PVDF membranes.

© 2026 FIMTEC & MPRL. All rights reserved.

* Corresponding author: 469493@qq.com (P. Fang)

DOI: 10.22079/jmsr.2025.2071653.1727

1. Introduction

The escalating severity of global environmental pollution and water scarcity has made developing efficient, low-energy water treatment technologies an urgent priority. Membrane separation technology [1-3] achieves substance separation through selective permeability, offering advantages including high efficiency, low energy consumption, simple operation, and excellent biocompatibility [4,5], demonstrating substantial application potential in environmental protection. Polyvinylidene fluoride (PVDF) membranes, recognized for their superior mechanical properties, chemical stability, and thermal stability, have become a prevalent choice for polymeric membrane materials, finding extensive use in water treatment and related fields.

Currently, the non-solvent induced phase separation (NIPS) method [6-9] represents the predominant approach for preparing PVDF microporous membranes. This process induces liquid-liquid or solid-liquid phase separation in the cast solution through solvent and non-solvent inter-diffusion [10,11], ultimately precipitating a polymer membrane with a specific pore network. However, the final structure and performance of PVDF membranes are synergistically influenced by complex interactions among multiple components—polymer, solvent, non-solvent, additives, and even nano-modifiers—constituting a typical multi-component, multi-physics coupled system. While traditional experimental methods can characterize the final membrane structure and properties, they struggle to capture in real-time and in situ the transient phase separation kinetics, microstructural evolution pathways, and synergistic mechanisms among components during film formation. This limited capacity to elucidate micro-mechanisms significantly hinders the targeted design and preparation efficiency of high-performance PVDF membranes.

Addressing these experimental limitations necessitates developing theoretical models and numerical simulation methods capable of revealing the microscopic mechanisms of the film-forming process. Phase-field simulation, an effective mesoscale numerical method, describes the distribution and spatiotemporal evolution of phases within a system using phase-field variables, enabling direct tracking of complex phase separation processes. Consequently, this study integrates the Cahn-Hilliard equation [12-15] and Flory-Huggins theory [16,17] to construct a phase-field model for the five-component PVDF/DMAc/H_2O/PVP/modifier system. The Cahn-Hilliard equation naturally describes diffusion kinetics during phase separation driven by chemical potential, while Flory-Huggins theory provides a reliable thermodynamic description for multicomponent polymer systems, quantifying component compatibility through interaction parameters.

Consequently, this study integrates the Cahn-Hilliard equation and Flory-Huggins theory to construct a phase-field model for the five-component PVDF/DMAc/H_2O/PVP/modifier system. It represents the first attempt to incorporate the synergistic effects between solvents and modifiers into a multicomponent phase separation kinetic analysis framework, utilizing numerical simulations to deeply investigate the microprocesses of immersion precipitation film formation. From a coupled thermodynamic-kinetic perspective, this research systematically analyzes the regulatory effects of different solvent types, modifier varieties, and concentrations on PVDF membrane microstructure formation. It aims to overcome traditional experimental characterization constraints, provide a novel theoretical perspective for understanding the PVDF membrane formation mechanism, and offer a solid theoretical basis and technical support for the precise and efficient preparation of high-performance PVDF membranes.

2. Model Development and Methodology

2.1. Establishment of the Membrane System Control Equation

(1) Law of Conservation of Mass

When modeling changes between systems using a quinary system approach, the mass conservation equation is employed to reflect actual material behavior and ensure the accuracy of physical processes. Components are represented as p (polymer), s (solvent), n (non-solvent), q (additive), and m (modifying agent).

The mass conservation equations between components are as follows:

$$\frac{\partial \phi_i}{\partial t}+\nabla\cdot(v\phi_i)=\nabla\cdot(D_i\nabla\phi_i)(i=p、\ s、\ n、\ q、\ m) \tag{1}$$

In the equation: ϕ_i — volume fraction; D_i — diffusion coefficient; v — convective velocity.

(2) Phase-field Evolution Equation

The state and distribution of phases are described by the evolution of phase field variables, and the phase separation process is driven by the chemical potential μ_i:

$$\frac{\partial \phi_i}{\partial t}=-\nabla\cdot\left(M_i\nabla\mu_i\right) \tag{2}$$

In the equation: M_i — mobility, controlling the rate of phase separation kinetics; μ_i — chemical potential.

$$\mu_i=\frac{\delta\mathcal{F}}{\delta\phi_i} \tag{3}$$

In the equation: $\mathcal{F}$ — the free energy of the system.

(3) Free Energy Functional

$$\mathcal{F}=\int_V\left[f\left(\phi_p,\phi_s,\phi_n,\phi_q,\phi_m\right)+\frac{\kappa}{2}|\nabla\psi|^2\right]dV \tag{4}$$

$$f=f_p(\phi_p)+f_s(\phi_s)+f_s(\phi_s)+f_q(\phi_q)+f_m(\phi_m) \tag{5}$$

In the equation: f — local free energy density.

(4) Solvent-Modifier Complex (s-m)

To reduce the complexity of the five-component system, the solvents (s) and modifiers (m) are treated as a composite, with their chemical potential μ_{s-m} and diffusion coefficient D_{s-m} described uniformly [18]:

$$D_{s-m}=D_{i0}\exp\left(-\frac{E_i}{RT}\right) \tag{6}$$

$$\mu_{s-m}=\frac{\partial f}{\partial\phi_{s-m}}-\kappa\nabla^2\phi_{s-m} \tag{7}$$

In the equation: D_{i0} — frequency factor; E_i — diffusion activation energy.

Treating the solvent and modifier as a composite entity (s-m) is a necessary strategy to balance computational complexity and physical realism. This assumption effectively captures their synergistic influence on the system's free energy, enabling successful prediction of macroscopic phase separation behavior and final membrane structure (as demonstrated in Chapter 3, showing good agreement with experiments). However, we acknowledge that this simplification may obscure the distinct kinetic roles of solvents and modifiers at the evolving polymer-nonsolvent interface. For instance, modifiers (e.g., GO, TiO_2) may exert unique kinetic functions independent of solvents through specific interfacial interactions or nucleation effects. The model describes a "synergistic net effect," providing a powerful macroscopic screening tool for high-performance membrane formulation design. Revealing finer, component-independent interfacial kinetic processes remains a key direction for future model development.

(5) Boundary and Initial Conditions

Three types of initial conditions were employed in the study:

①Uniform initial conditions in the format $\phi_s+0.05$, $\phi_p+0.05$, $\phi_p+0.005$, and $\phi_{s-m}+0.005$ for the five-component system;

②Two-layer initial conditions (polymer solution layer + coagulation bath layer), with uniform concentration distribution within each layer, used in most membrane simulations;

③Partial membrane simulations employed two-layer initial conditions with non-uniform concentration distribution within each layer to capture the evaporation of volatile solvents.

Boundary conditions:

$$\left.\frac{\partial\phi_i}{\partial y}\right|_{y=0}=0,\left.\frac{\partial\mu_i}{\partial y}\right|_{y=0}=0 \tag{8}$$

Express the conservation equation as the divergence of flux:

$$\frac{\partial\phi_i}{\partial t}=-\nabla\cdot\vec{J}_i=-\left(\frac{\partial J_{ix}}{\partial x}+\frac{\partial J_{iy}}{\partial y}+\frac{\partial J_{iz}}{\partial z}\right) \tag{9}$$

Linear extrapolation is used at the boundary as the second boundary condition for the fourth-order partial differential equation:

$$\frac{\partial^2\phi_i}{\partial y^2}=0 \tag{10}$$

Table 1
Flory-Huggins Interaction Parameters χ_{ij} in the System

System	Volume fraction %	$\chi_{n(s-m)}$	$\chi_{(s-m)p}$	χ_{np}	χ_{nq}	$\chi_{(s-m)q}$	χ_{pq}
PVP/PVDF/DMAc/H_2O/TiO_2	2/18/74/5/1	0.21	0.17	0.97	0.33	0.21	0.82
	2/18/73/5/2	0.23	0.17	0.98	0.35	0.21	0.81
	2/18/72/5/3	0.19	0.19·	0.97	0.33	0.22	0.84
PVP/PVDF/DMAc/H_2OPDA	2/18/74/5/1	0.23	0.18	0.55	0.54	0.77	0.85
	2/18/73/5/2	0.22	0.16	0.63	0.54	0.72	0.83
	2/18/72/5/3	0.24	0.15	0.52	0.43	0.65	0.88
PVP/PVDF/DMAc/H_2O/GO	2/18/74.8/5/1.2	0.31	0.21	0.32	0.83	0.75	0.35
	2/18/74.7/5/1.3	0.29	0.23	0.29	0.88	0.77	0.33
	2/18/74.6/5/1.4	0.33	0.27	0.33	0.85	0.72	0.39

In summary, the following control equation can be derived:

$$\frac{\partial \varphi_{s-m}}{\partial t} = M_{(s-m)(s-m)}(s-m)\nabla^2\left[\begin{array}{l}\dfrac{\partial f}{\partial \varphi_{s-m}} - K_{(s-m)(s-m)}\nabla^2\varphi_{s-m} - \dfrac{1}{2}(K_{(s-m)p} + K_{p(s-m)})\nabla^2\varphi_p \\ -\dfrac{1}{2}(K_{(s-m)q} + K_{q(s-m)})\nabla^2\varphi_q\end{array}\right] + M_{(s-m)p}\nabla^2\left[\frac{\partial f}{\partial \varphi_p} - K_{pp}\nabla^2\varphi_p - \frac{1}{2}(K_{(s-m)p} + K_{p(s-m)})\nabla^2\varphi_{s-m} - \frac{1}{2}(K_{pq} + K_{qp})\nabla^2\varphi_q\right] + M_{(s-m)q}\nabla^2\left[\frac{\partial f}{\partial \varphi_q} - K_{qq}\nabla^2\varphi_q - \frac{1}{2}(K_{(s-m)q} + K_{q(s-m)})\nabla^2\varphi_{s-m} - \frac{1}{2}(K_{pq} + K_{qp})\nabla^2\varphi_p\right] \quad (1)$$

$$\frac{\partial \varphi_p}{\partial t} = M_{p(s-m)}\nabla^2\left[\begin{array}{l}\dfrac{\partial f}{\partial \varphi_{s-m}} - K_{(s-m)(s-m)}\nabla^2\varphi_{s-m} - \dfrac{1}{2}\left(K_{(s-m)p} + K_{p(s-m)}\right)\nabla^2\varphi_p \\ -\dfrac{1}{2}\left(K_{(s-m)q} + K_{q(s-m)}\right)\nabla^2\varphi_q\end{array}\right] + M_{pp}\nabla^2\left[\frac{\partial f}{\partial \varphi_p} - K_{pp}\nabla^2\varphi_p - \frac{1}{2}\left(K_{(s-m)p} + K_{p(s-m)}\right)\nabla^2\varphi_{s-m} - \frac{1}{2}\left(K_{pq} + K_{qp}\right)\nabla^2\varphi_p\right] + M_{pq}\nabla^2\left[\frac{\partial f}{\partial \varphi_q} - K_{(s-m)(s-m)}\nabla^2\varphi_q - \frac{1}{2}\left(K_{(s-m)q} + K_{q(s-m)}\right)\nabla^2\varphi_{s-m} - \frac{1}{2}\left(K_{pq} + K_{qp}\right)\nabla^2\varphi_p\right] \quad (2)$$

$$\frac{\partial \varphi_q}{\partial t} = M_{q(s-m)}\nabla^2\left[\begin{array}{l}\dfrac{\partial f}{\partial \varphi_{s-m}} - K_{(s-m)(s-m)}\nabla^2\varphi_{s-m} - \dfrac{1}{2}\left(K_{(s-m)p} + K_{p(s-m)}\right)\nabla^2\varphi_p \\ -\dfrac{1}{2}\left(K_{(s-m)q} + K_{q(s-m)}\right)\nabla^2\varphi_q\end{array}\right] + M_{pp}\nabla^2\left[\frac{\partial f}{\partial \varphi_p} - K_{pp}\nabla^2\varphi_p - \frac{1}{2}\left(K_{(s-m)p} + K_{p(s-m)}\right)\nabla^2\varphi_{s-m} - \frac{1}{2}\left(K_{pq} + K_{qp}\right)\nabla^2\varphi_p\right] + M_{qq}\nabla^2\left[\frac{\partial f}{\partial \varphi_q} - K_{qq}\nabla^2\varphi_q - \frac{1}{2}\left(K_{(s-m)q} + K_{q(s-m)}\right)\nabla^2\varphi_{s-m} - \frac{1}{2}\left(K_{pq} + K_{qp}\right)\nabla^2\varphi_p\right] \quad (3)$$

2.2. Model assumptions

(1) Assume the system is in thermodynamic equilibrium within a local region, with the evolution of phase-field variables driven by local free energy;

(2) Assume the total volume of all components in the system remains conserved during evolution;

(3) The phase-field model assumes finite interface widths, where the mesoscale interface thickness is typically much larger than the molecular scale;

(4) Simplified energy functionals (Flory-Huggins type) are employed to describe interactions between components, and the model neglects certain complex intermolecular electrostatic forces;

(5) In some cases, the kinetic pathways during phase separation or structural evolution are assumed reversible, ignoring irreversible phenomena such as aging and degradation;

(6) Mobility is assumed to depend solely on concentration or constants [19-21].

(7) Explanation Regarding Thermodynamic-Kinetics Coupling and Process Irreversibility

While the fundamental dynamical equations are mathematically reversible, our model effectively captures the irreversibility of the NIPS process through two key aspects: ①The thermodynamic drive from a metastable homogeneous state to a phase-separated state is unidirectional. ②In the simulation, the polymer phase is considered 'frozen' once its concentration surpasses a critical threshold (e.g., gel point), thereby locking in the non-equilibrium membrane structure. The 'thermodynamic-kinetic coupling' is realized through a specific feedback mechanism: the local composition determines the free energy density and chemical potential gradient (thermodynamic driving force), which governs the diffusion flux (kinetic response). This flux alters the local composition, which in turn updates the free energy landscape. This continuous, dynamic interplay—particularly the positive feedback instability during initial phase separation—is crucial for the model's ability to replicate microstructural evolution mechanisms.

2.3. Numerical Implementation

2.3.1. Grid Method and Central Difference Method

The computational domain is discretized into a uniform grid of 150 × 300 cells (physical dimensions 125 nm × 250 nm) using an equidistant partitioning strategy (spatial resolution $\Delta x = \Delta y = 1$ non-dimensional units). Central differences are employed to approximate derivatives, yielding the finite difference equations:

$$\frac{k_{x,i+\frac{1}{2},j}(u_{i+1,j} - u_{i,j}) - k_{x,i-\frac{1}{2},j}(u_{i,j} - u_{i-1,j})}{\Delta x^2} + \frac{k_{y,i,j+\frac{1}{2}}(u_{i,j+1} - u_{i,j}) - k_{y,i,j-\frac{1}{2}}(u_{i,j} - u_{i,j-1})}{\Delta y^2} + S_{i,j} = 0 \quad (4)$$

Grid quality was assessed to ensure computational accuracy and reliability. The characteristic length of the uniform grid was 1 dimensionless unit (~0.83 nm physically), resolving the typical interface thickness (1–10 nm) during PVDF membrane formation. All grid cells exhibited excellent orthogonality (>0.9) and low skewness (<0.1), far exceeding common engineering thresholds, thus ensuring numerical stability and avoiding spurious oscillations. The uniform aspect ratio of 1 guaranteed consistent accuracy across the domain, meeting the grid quality requirements for phase-field simulations [22,23].

2.3.2. Algorithm Implementation

Simulations were performed in two dimensions using the FiPy numerical package, a Python-based tool for solving partial differential equations via the finite volume method. FiPy was developed by the National Institute of Standards and Technology (NIST), including contributions from the Materials Measurement Laboratory (MML) and the Center for Theoretical and Computational Materials Science (CTCMS), providing a robust framework for phase-field modeling [24-25].

The choice of 2D simulation represents a balance between computational efficiency and the capture of essential physical mechanisms, facilitating extensive parameter sensitivity studies. The 2D approach successfully reveals cross-sectional membrane structure formation and allows qualitative comparison with experimental SEM images. Future work will extend to 3D simulations to more comprehensively investigate gradient structures and pore connectivity through the membrane thickness.

2.4. Experimental Validation Design

2.4.1. Materials and Instruments

(1) Materials: Using polyvinylidene fluoride (PVDF, grade FR904) as the substrate, N, N-dimethylacetamide (DMAc), N, N-dimethylformamide (DMF), triethyl phosphate (TEP) as solvents, polyvinylpyrrolidone (PVP) as an additive, graphene oxide (GO), titanium dioxide (TiO_2), and polydopamine (PDA) as modifying agents, bovine serum albumin (BSA) for retention testing, and pure water as the non-solvent and testing medium.

(2) Instrumentation: Includes vacuum drying oven, ultrasonic cleaner, constant-temperature magnetic stirrer, contact angle measuring instrument, UV spectrophotometer, high-pressure flat-plate membrane pilot tester, Fourier Transform Infrared Spectrometer (Bruker-TESO II), Field Emission Scanning Electron Microscope (Hitachi-s-470), etc., to meet requirements for membrane fabrication, performance testing, and structural characterization.

2.4.2. PVDF Membrane Preparation Process (NIPS Method)

Modified PVDF membranes were prepared using the NIPS method, employing PVDF (FR904) as the substrate and incorporating solvents such as DMAc/DMF/TEP, PVP additives, and GO/ TiO_2/PDA modifying agents. PVDF, additives, and modifiers were mixed according to the formulation and ultrasonically dispersed for 60 minutes. Solvent was added, followed by stirring at 60°C for 30 minutes and then at 80°C for 12 hours, followed by standing at 80°C for 8 hours to remove bubbles, yielding the casting solution. The solution

was coated onto glass substrates using a 200μm squeegee, left to stand for 15 seconds, then immersed in a 20°C deionized water coagulation bath for 10 days (with water replaced as needed) to complete the phase inversion [26,27]. By adjusting the solvent type, modifier type, and their volume fraction (GO 0.2%-0.6%, TiO_2 2.5%-4.5%, PDA 0.6%-1.4%), the membrane's structural properties can be controlled.

Model-predicted pore morphology (size, distribution, skin layer thickness) was directly compared with experimental SEM images. Bulk performance metrics like water flux and rejection rate were used for quantitative validation. While rejection is also influenced by surface chemistry and charge, this model primarily establishes the critical link between morphology and selectivity by accurately predicting average pore size and distribution. The observed experimental trends—such as simultaneous improvement in flux and rejection with GO-induced pore uniformity—support this structural correlation.

It is important to clarify that this phase-field model primarily establishes a predictive bridge from film formation kinetics to microscopic pore morphology (e.g., pore size, distribution, skin layer thickness), which forms the core link to membrane performance (water flux, rejection). This correlation is based predominantly on the physical size exclusion mechanism. We fully acknowledge that actual rejection rates are also affected by surface properties introduced by modifiers. In the current model, these surface effects are partially and indirectly incorporated via their influence on phase separation thermodynamics (through Flory-Huggins parameters) and the resulting membrane structure. The model's strong agreement with experimental data suggests that pore morphology is the dominant performance-governing mechanism in the studied systems. The current model serves as a quantitative tool for structure-based performance optimization, while explicit incorporation of surface physicochemical properties is a key direction for future refinement.

3. Results and Discussion

3.1 Effects of Different Solvents on Membrane Structure and Properties

This study selected three common solvents (DMF, DMAc, TEP) and successfully prepared three distinct types of PVDF membranes via a phase inversion process. Detailed morphological and structural analyses were conducted on these membranes before and after use, and systematic investigations and comparisons were performed on changes in their physicochemical properties, including water flux, rejection rate, and hydrophilicity.

3.1.1. Analysis of Two-Dimensional Simulation Results Under Different Solvents

As shown in the simulation results of Fig. 1, when DMF is used as the solvent, the membrane has a dense structure with fewer and smaller pores, and the phase separation process is predominantly delayed with a slow rate [28,29]. When DMAC serves as the solvent, the membrane exhibits a dense outer layer with moderate pore number and size in the subsurface layer, resulting in phase separation between instantaneous and delayed separation with a steady separation rate. When TEP is used as the solvent, the outer layer is thinner, featuring numerous large pores in the subsurface layer, predominantly exhibiting instantaneous phase separation with a rapid separation rate. Within the same timeframe, the order of membrane pore number and size is TEP > DMAC > DMF. As shown in Fig. 2, the DMF-formed membrane exhibits a smooth and dense surface with a cross-section revealing a finger-like pore structure; the DMAC-formed membrane has a slightly rough surface with a cross-section displaying a double-continuous porous structure; the TEP-formed membrane features a rough and porous surface with a cross-section exhibiting a sponge-like pore structure.

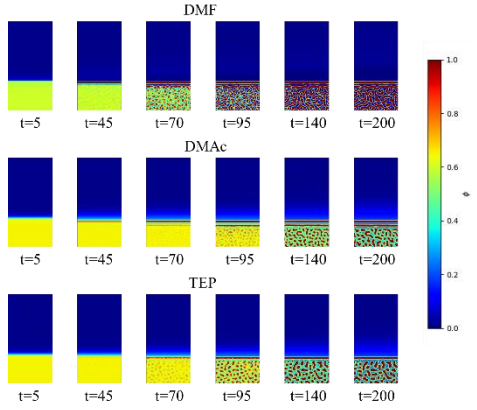


Fig. 1. Microscopic simulation results of the PVDF membrane system in a quinary system under different solvent conditions.

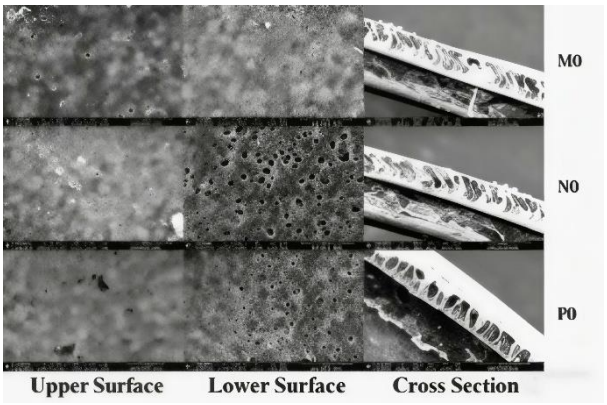


Fig. 2. Effect of different solvents on the structure of PVDF blend membranes.

Experimental validation results (Table 2) show that DMF has the lowest water flux, porosity, and average pore size, but the highest rejection rate; TEP shows the opposite characteristics; and DMAc's performance metrics lie between the two, which is consistent with the simulation results [30,31]. When TEP served as the solvent, its minimal solubility parameter difference ($\delta_p - \delta_s = 1.05 MPa^{1/2}$) with PVDF led to reduced casting solution stability due to weak interactions. Rapid permeation of the non-solvent (water) triggered instantaneous phase separation, forming sponge-like macropores (Fig. 2). In contrast, the strong interactions ($\delta_p - \delta_s = 2.46 MPa^{1/2}$) between DMF and PVDF delayed phase separation. The densification of the skin layer restricted pore growth (water flux only 653.28 $L/m^{-2}\cdot h^{-1}$).

Table 2
Effect of different solvents on the performance of PVDF blend films.

Solvent type	water flux J_W ($L/m^{-2}\cdot h^{-1}$)	Retention rate R_0 (%)	porosity ε_0 (%)	average pore size r_m (nm)
DMF	653.28	72.65	71.33	22.35
DMAc	795.36	75.36	73.68	22.65
TEP	826.37	68.59	85.24	23.26

3.1.2 Analysis of Film Formation Processes Under Different Solvents

The thermodynamic phase diagram in Fig. 3 shows that the phase separation lines for all three solvents shift toward the solvent/non-solvent axis, resulting in a reduced homogeneous region. DMF exhibits the strongest interaction with PVDF, with its phase boundary residing in the high non-solvent concentration region, indicating a tendency toward delayed phase separation. DMAc shows weaker interaction, shifting its phase boundary toward the low non-solvent concentration region, suggesting partial instantaneous phase separation. TEP demonstrates the weakest interaction, with its phase boundary closest to the non-solvent concentration axis, indicating a tendency toward instantaneous phase separation.

Kinetically, solvent viscosity affects phase separation time, with DMF exhibiting the highest viscosity and TEP the lowest. Membrane shell formation is primarily governed by solid-liquid phase transitions and controlled by mass transfer coefficients. Subshell formation is thermodynamically influenced, dominated by liquid-liquid coexistence phase transitions. In summary, DMF is suitable for high retention scenarios, TEP for high water flux scenarios, and DMAc offers a balanced approach for both [32,33].

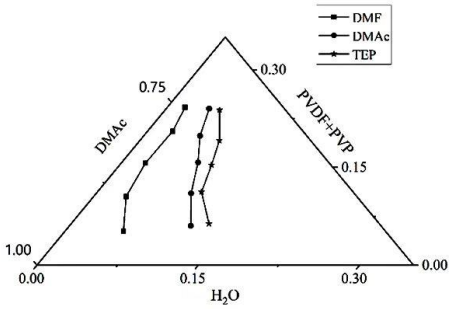


Fig. 3. Phase diagram of five-component PVDF blend membranes under different solvent conditions.

3.2. Synergistic Regulatory Mechanism of Modified Substances

3.2.1. Analysis of Two-Dimensional Simulation Results Under Different Modification Agents

Fig. 4 shows that with GO addition, the film exhibits uniform pore distribution with a high pore count, small crystal size, thin skin layer, and short film formation time. With TiO_2 addition, the film features relatively uniform pore distribution, slightly larger crystal size, moderate skin layer thickness, and slightly longer film formation time. With PDA addition, the film displays uneven pore distribution, large crystal size, thick skin layer, and prolonged film formation time. GO yields the optimal effect, followed by TiO_2, while PDA performs the least effectively [34,35].

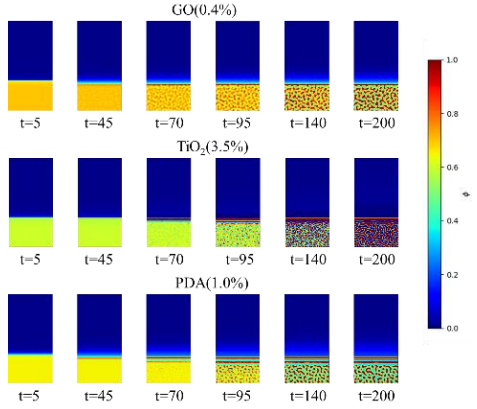


Fig. 4. Microscopic simulation of a PVDF membrane system in a quinary system under different types of modified substances.

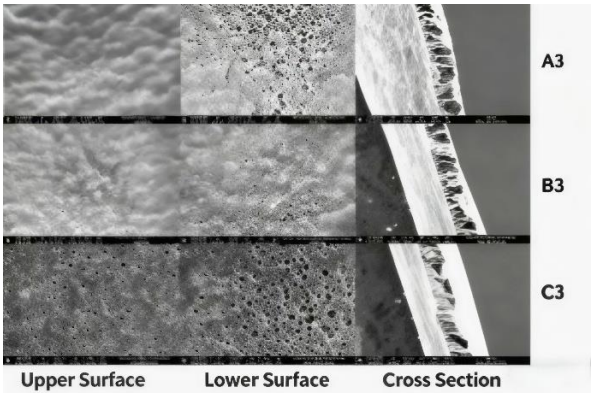


Fig. 5. Effect of different types of modified substances on the structure of PVDF blend membranes.

Table 3 shows that GO enhances water flux, rejection rate, and porosity while reducing the average pore size; TiO_2 excels in improving rejection rate; PDA constructs a dense structure that affects water flux and other properties, consistent with simulation results [36,37]. Fig. 5 reveals that the GO-modified membrane exhibits a smooth, dense surface with protrusions and a cross-section of uniformly interconnected sponge-like pores. The TiO_2-modified membrane surface is uniformly slightly rough, with a cross-section featuring both finger-like and sponge-like pores. The PDA-modified membrane surface comprises a thick, dense, layered crust, exhibiting large and uneven sublayer pores in cross-section.

Table 3
Effect of different types of modified substances on the properties of PVDF blend films.

Number	water flux J_W ($L/m^{-2}\cdot h^{-1}$)	Retention rate R_0 (%)	porosity ε_0 (%)	average pore size r_m (nm)
GO	895.64	87.35	82.35	29.81
TiO_2	836.25	89.23	74.12	32.54
PDA	805.33	88.36	65.67	31.23

3.2.2. Film Formation Processes of Different Types of Modified Substances

The thermodynamic phase diagram in Fig. 6 shows that TiO_2 shifts the phase boundary toward the low non-solvent concentration region, leading to partial instantaneous phase separation; GO positions the phase boundary closest to the non-solvent concentration axis, favoring instantaneous phase separation; PDA places the phase boundary in the high non-solvent concentration region, favoring delayed phase separation. Thermodynamically, TiO_2 enhances interfacial bonding, forming a coexisting structure of finger-like and sponge-like pores; GO optimizes molecular arrangement, creating a uniformly interconnected porous structure; PDA increases toughness, forming a thick crust and non-uniform pore structure. Kinetically, all three increase system viscosity and delay diffusion. TiO_2 moderates shell formation time, enabling simultaneous liquid-liquid and solid-liquid phase separation in the sublayer; GO shortens shell formation time, causing instantaneous phase separation in the sublayer; PDA prolongs shell formation time, inducing delayed phase separation in the sublayer [38,39].

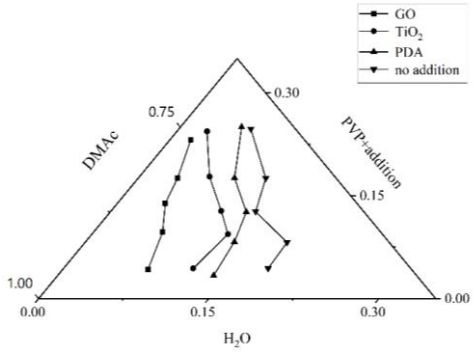


Fig. 6. Phase diagram of H2O/DMAc/PVDF/PVP/GO blend membranes under different types of modified substances.

3.2.3. The Effect of Different GO Volume Fractions

Fig. 7 simulates the evolution of membrane structure at GO volume fractions of 0.3%, 0.4%, and 0.6%. At 0.3%, the phase separation onset point is slightly advanced, with minimal impact on membrane structure. At 0.4%, the phase separation process is significantly altered, leading to substantial changes in membrane structure. At 0.6%, agglomeration causes uneven pore distribution, demonstrating the influence of GO volume fraction on phase separation and membrane structure. Fig. 8 presents the effects of GO volume fraction on membrane water flux and rejection rate. Below 0.3% GO volume fraction, water flux increases with GO content (maximum increase of 42%), while rejection rate gradually rises. Above 0.4%, GO agglomeration causes water flux to decrease. At 0.6%, rejection rate reaches its maximum, demonstrating the regulatory role of GO volume fraction on membrane separation performance [40,41].

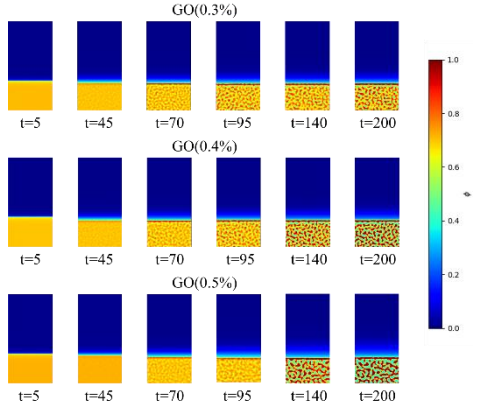


Fig. 7. Microstructural simulation of a PVDF membrane system in a quinary system under different GO volume fraction conditions.

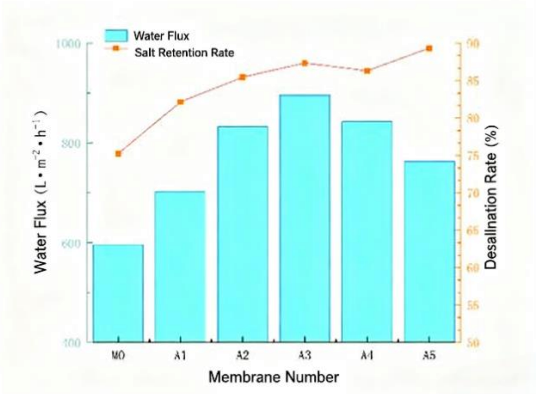


Fig. 8. Changes in water flux and retention rate of PVDF membranes under different GO volume fractions.

Fig. 9 SEM images reveal the surface and cross-sectional morphology of the membrane at different GO volume fractions. At low volume fractions, the membrane surface appears smooth with numerous uniformly distributed pores. At 0.4%, pores are evenly dispersed, and cross-sections exhibit finger-like pores penetrating the membrane interior. At 0.5%, GO agglomeration occurs, resulting in a relatively dense membrane structure, validating the influence of GO volume fraction on the membrane microstructure as simulated. Fig. 10: Fourier transform infrared (FTIR) spectrum. The peak at 1830 cm^{-1} corresponds to the stretching vibration of the C=O double bond in the carboxyl groups of GO, while the peak at 1560 cm^{-1}corresponds to the vibration of the C=C double bonds and O-H bonds in GO. The peak at 1270 cm^{-1} represents the stretching vibration peak of C-O double bonds in GO epoxy groups, confirming the successful blending of GO into the PVDF membrane and the introduction of hydrophilic groups.

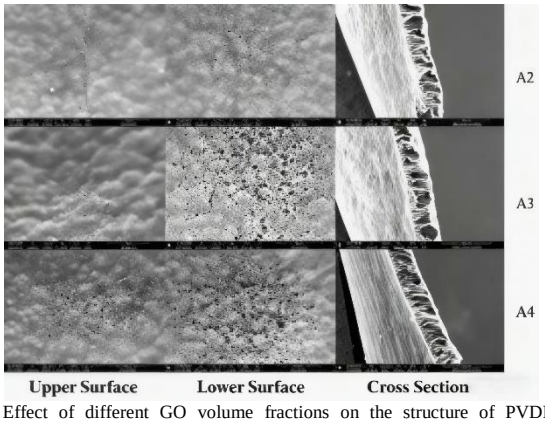


Fig. 9. Effect of different GO volume fractions on the structure of PVDF blend membranes.

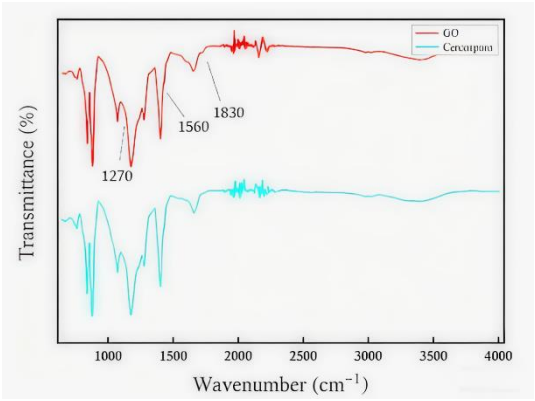


Fig. 10. Infrared spectrum of the membrane surface at a GO volume fraction of 0.4%.

Fig. 11 combines bar and line charts to illustrate the effects of GO volume fraction on membrane porosity and average pore size. Porosity increases continuously with rising GO volume fraction, peaking at 0.6%. Average pore size first increases then decreases, reaching a maximum of 37.12 nm at 0.2% and dropping to 28.35 nm at 0.6%, reflecting GO's regulatory pattern on membrane pore structure. Fig. 12 demonstrates that GO addition significantly enhances membrane hydrophilicity. However, as the GO volume fraction increases, the contact angle progressively decreases, indicating progressively stronger hydrophilicity. Yet, when the GO volume fraction exceeds 0.4%, the contact angle increases, suggesting agglomeration occurs, which reduces membrane hydrophilicity. This also corroborates the simulated increase in impurities and the experimentally observed decrease in water flux.

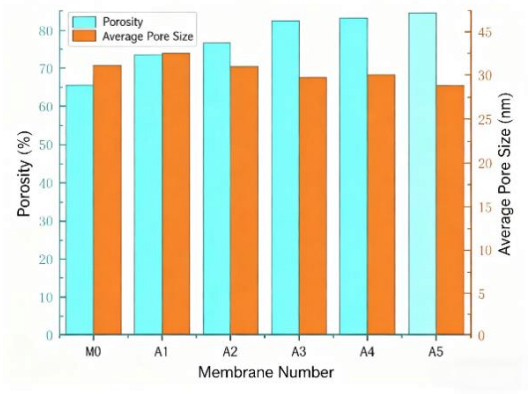


Fig. 11. Comparison of pore volume fraction and average pore diameter of modified membranes under different GO volume fraction conditions.

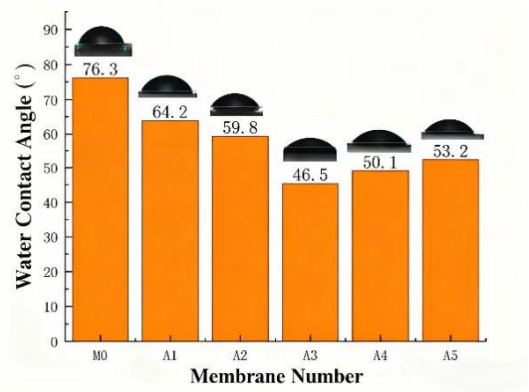


Fig. 12. Contact angle of PVDF membrane under different GO volume fractions.

3.2.4. Effect of Different TiO2 Volume Fractions

Fig. 13 simulations show that at a TiO_2 volume fraction of 3.0%, particles are sparse with gradual phase separation, resulting in fewer but uniform pores. At 3.5%, increased particle density leads to complete phase separation, yielding

numerous uniform pores with superior performance. At 4.0%, particle agglomeration causes large and non-uniform pores, reducing overall uniformity. Fig. 14 presents a line chart illustrating the effect of TiO_2 volume fraction on membrane water flux and rejection rate. At 3.0%, water flux increases while rejection rate remains largely unchanged; at 3.5%, both water flux and rejection rate reach optimal levels; at 4.0%, rejection rate further increases but water flux decreases due to uneven pore distribution. This indicates that 3.5% is the optimal volume fraction of TiO_2.

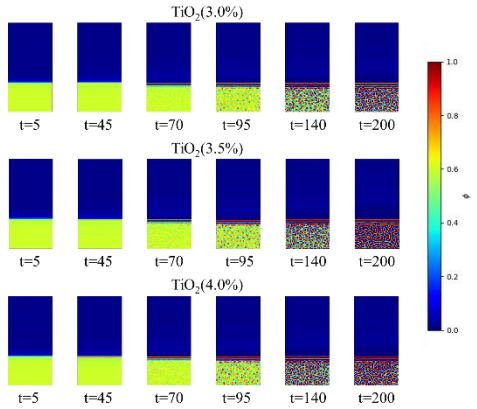


Fig. 13. Microstructural simulation of a PVDF membrane system in a quinary system under different TiO_2 volume fractions.

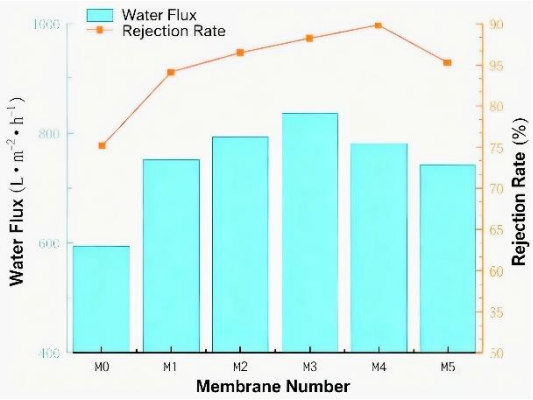


Fig. 14. shows the changes in water flux and retention rate of PVDF membranes at different TiO_2 volume fractions.

Fig. 15 SEM images reveal the surface and cross-sectional morphologies of membranes at different TiO_2 volume fractions. At 3.0%, the membrane pore density increases; at 3.5%, the highest pore density is observed with an asymmetric finger-like pore structure in cross-section. At 4.0%, TiO_2 agglomerates appear on the membrane surface, reducing pore size and forming bubble-like pores in cross-section due to agglomeration, validating the simulated effect of TiO_2 volume fraction on membrane structure. Fig. 16: Infrared spectrum. The peak at 927 cm^{-1} corresponds to the Ti-O bond vibration of TiO_2, confirming its successful incorporation. The characteristic peaks of the α-phase PVDF (1233 cm^{-1}, 1395 cm^{-1}) show reduced intensity, while the peak of the β-phase (1640 cm^{-1}) exhibits significantly enhanced intensity. This indicates that TiO_2 promotes the phase transition of PVDF from the α-phase to the β-phase.

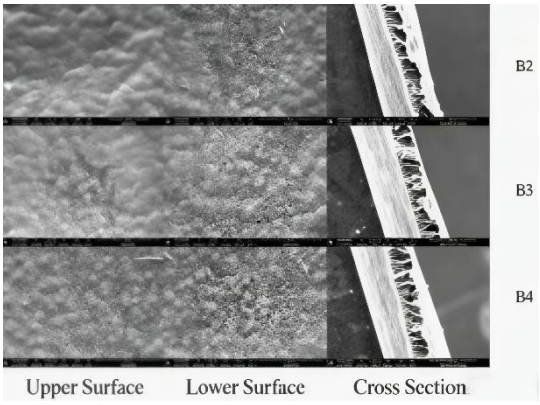


Fig. 15. Effect of different TiO_2 volume fractions on the upper structure of PVDF blend membranes.

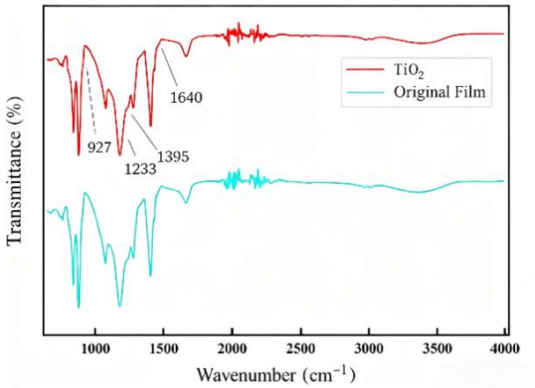


Fig. 16. Infrared spectrum of the membrane surface at a TiO_2 volume fraction of 3.5%.

As shown in Fig. 17, the volume fraction of TiO_2 significantly influences the membrane porosity and average pore size: porosity first increases then decreases with increasing TiO_2 content (68.2% at 2.5%, peaks at 74.83% at 4.0%, and drops to 71.3% at 4.5%); while the average pore size increases initially and then decrease (maximum of 33.26 nm at 3.0%, dropping to 31.26 nm at 4.5%). At low TiO_2 content (≤3.0%), uniform dispersion promotes phase separation; at moderate content (3.5%–4.0%), pore expansion and dispersion are balanced; beyond 4.0%, particle agglomeration blocks the pores. In Fig. 18, the contact angle of pure PVDF membranes was 76.3°. Adding TiO_2 caused a continuous decrease, reaching a minimum of 51.6° at 3.0% and slightly recovering to 57.5% at 4.5%. The enhanced hydrophilicity resulted from hydrogen bonding formed by TiO_2 hydroxyl groups and induced phase transition to the PVDF β-phase. Optimal dispersion was achieved at 3.0%, while excess TiO_2 caused agglomeration that masked hydrophilic groups, consistent with SEM observations.

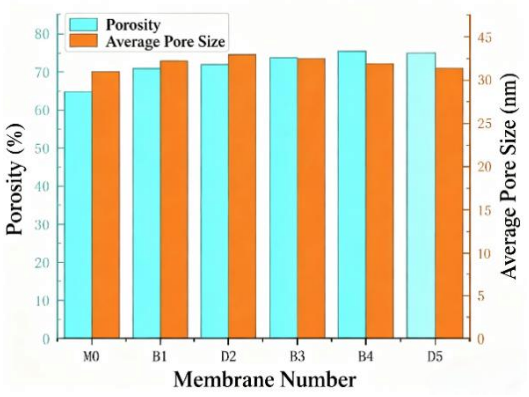


Fig. 17. Comparison of modified membrane porosity and average pore size under different TiO_2 volume fractions.

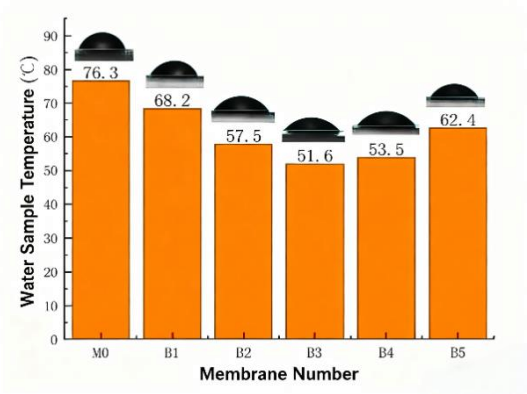


Fig.18. Contact angle of PVDF membrane under different TiO_2 volume fractions.

3.2.5. Effect of Different PDA Volume Fractions

Fig. 19 simulations indicate that at 0.8% PDA content, it disperses as small aggregates with minimal impact on phase separation and uniform pore distribution. At 1.0%, it forms a continuous network that delays mass transfer, transforming finger-like pores into regular cavities while densifying the cortex. At 1.2%, severe agglomeration compresses the pore channels, damaging surface and sublayer pore structures. PDA modulates phase separation through interfacial adsorption. At optimal levels, it balances structural density and connectivity; excess leads to defects. Fig. 20 shows water flux initially increases then decreases with PDA addition, peaking at 805.33 $L/m^{-2}\cdot h^{-1}$ at 1.0%. Retention rate continuously improves, reaching 89.6% at 1.4%. Within the 0.6%–1.0% range, PDA introduces hydrophilic groups that enhance flux; optimal synergy between hydrophilicity and pore structure occurs at 1.0%. Beyond this concentration, pore blockage causes flux decline, reflecting a typical "flux-rejection" trade-off relationship.

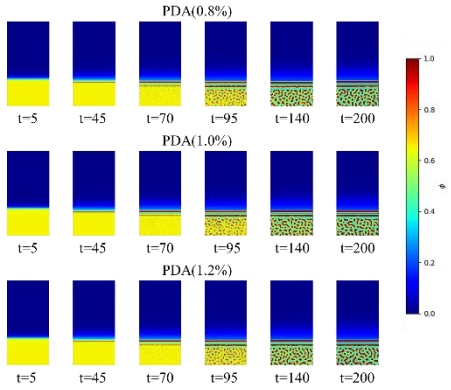


Fig. 19. Microstructural simulation of the PVDF membrane system in a quinary system under different PDA volume fractions.

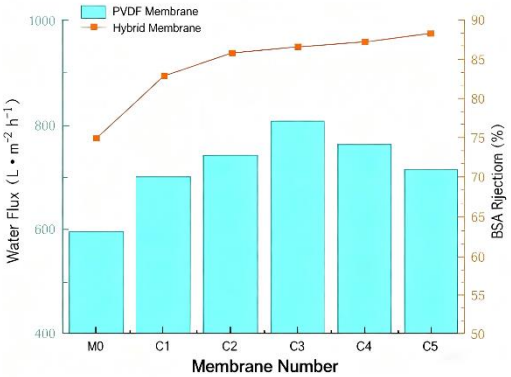


Fig. 20. Variation in water flux and rejection rate of the PVDF membrane at different PDA volume fractions.

Fig. 21 demonstrates that the volume fraction of PDA significantly influences membrane structure: at 0.8%, the surface is smooth with a typical asymmetric cross-sectional structure; at 1.0%, the surface pore size is uniform, with regular finger-like pores and a denser skin layer; at 1.2%, layered irregularities appear on the surface, and finger-like pores are filled by PDA. This indicates that an appropriate PDA content (1.0%) optimizes the structure, while excessive amounts induce defects. In Fig.22, the infrared spectrum of the 1.5% PDA-containing membrane exhibits characteristic PDA peaks at 1632 cm^{-1} and 3416 cm^{-1}, overlapping with PVDF peaks. This confirms excellent molecular compatibility between the two materials, providing chemical evidence for structural stability.

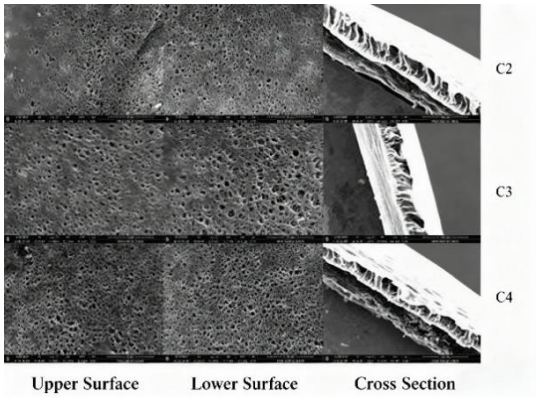


Fig. 21. Effect of Different PDA Volume Fractions on the Superstructure of PVDF Blended Membranes.

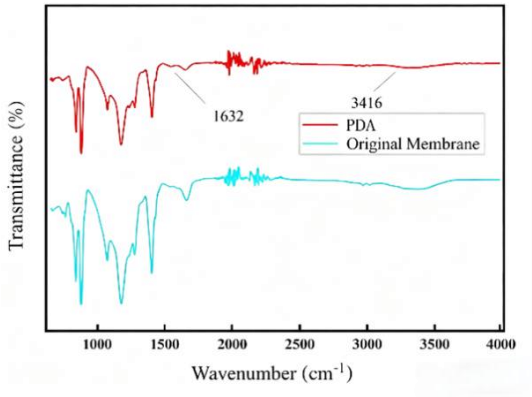


Fig. 22. Infrared Spectrum of the Membrane Surface at 1.5% PDA Volume Fraction.

Fig. 23 shows that the PDA volume fraction has a minor effect on membrane porosity (65%–68%) and average pore size (30.5–31.8 nm), both of which remain close to those of the pure membrane. This indicates that PDA primarily coats pore surfaces with nanolayers without altering the overall pore structure of the membrane, consistent with its interfacial modification mechanism. In Fig. 24, the contact angle first decreases then increases with PDA addition, reaching its minimum (53.2°) at 1.0% before rebounding to 56.3° due to agglomeration. This trend correlates with water flux variations, indicating optimal PDA dispersion and hydrophilicity at 1.0%. This further validates this concentration as the optimal performance condition.

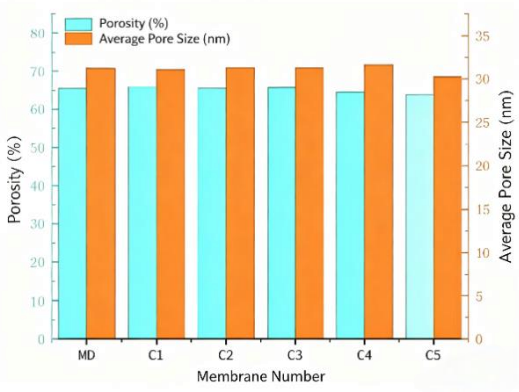


Fig. 23. Comparison of modified membrane porosity and average pore size under different PDA volume fractions.

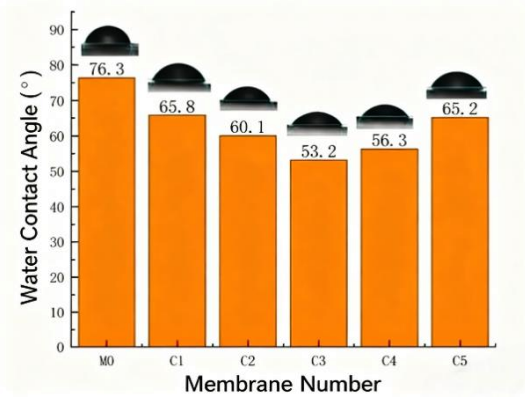


Fig. 24. Contact angle of PVDF membranes at different PDA volume fractions.

3.3. Model Parameter Sensitivity Analysis

Sensitivity analysis primarily investigates the effects of migration rate, gradient loss coefficient, and interfacial energy coefficient on film structure evolution:

Migration rate: It mainly governs the temporal scale of film formation kinetics and has a relatively weak direct impact on the final film structure. A high migration rate accelerates phase separation, favoring the formation of large pores with good connectivity but uneven distribution; a low migration rate slows down phase separation, promoting the formation of small pores with uniform distribution.

Gradient Loss Coefficient: Significantly controls the microstructure of the film. Lower values yield more desirable simulation results. At low coefficients, the film exhibits enhanced structural integrity and shorter formation times, presenting a multiscale structure with both reticular pores and large pores. At high coefficients, the film formation kinetics are delayed, resulting in a structure dominated by large pores.

Interfacial Energy Coefficient: Simultaneously influences phase separation kinetics, pore structure characteristics, and crystallization behavior. A value of 0.25 yields optimal crystallization growth rates while achieving excellent crystalline integrity and membrane compactness [42-44].

4. Conclusion

This study successfully established a phase-field model for a quinary PVDF membrane system based on the Cahn-Hilliard equation and Flory-Huggins theory, systematically simulating and revealing the phase separation behavior and microstructural evolution mechanisms during the immersion precipitation membrane fabrication process. This model effectively quantifies the synergistic interactions between solvents and modifiers in multicomponent systems. Its predictions regarding the formation of asymmetric membrane structures and key performance indicators show excellent agreement with experimental observations, with deviations below 5%.

Key contributions of this study include:

(1) Model Innovation: Established a phase-field kinetic model capable of handling the pentary PVDF/DMAc/H_2O/PVP/modifying agent system. This model integrates solvent-modifying agent synergistic effects into a unified phase-separation kinetic framework for the first time, overcoming limitations of traditional models in handling complex compositions.

(2) Mechanism Elucidation: Through thermodynamic-kinetic coupling analysis, we elucidated the microscopic physical mechanisms by which different solvents (DMF, DMAc, TEP) influence membrane pore structure via regulating phase separation rates (delayed/instantaneous). We also revealed the intrinsic rules governing how modifiers (GO, TiO_2, PDA) modulate membrane performance by optimizing molecular arrangement and inducing crystalline phase transitions.

(3) Quantitative Guidance: The model determines that GO at 0.4% volume fraction achieves optimal membrane pore uniformity and performance (water flux: 895.64 $L \cdot m^{-2} \cdot h^{-1}$; rejection rate: 87.35%), while TiO_2 at 3.5% exhibits the best overall performance by promoting PVDF β-phase formation. This provides a precise quantitative optimization tool for formulating high-performance PVDF membranes.

Based on the findings and insights from this study, the following prospects are proposed for future research:

(1) Model Dimension Expansion: The current two-dimensional model can be further developed into a three-dimensional simulation to more realistically reveal the gradient pore structure in the membrane thickness direction and its impact on mass transfer efficiency.

(2) Deepening physical field coupling: Future work may incorporate the dynamic influence of temperature fields on diffusion coefficients and phase equilibrium, while considering the direct effects of surface chemistry (e.g., hydrophilicity, charge effects) on selectivity and anti-fouling performance, thereby establishing a more comprehensive “structure-property” relationship.

Acknowledgments

This research was completed with valuable support and assistance from many individuals. Additionally, we appreciate those who helped with language polishing and paper proofreading, which ensured the smooth completion of this study. This research did not receive any specific grant from funding agencies in the public, commercial, or not-for-profit sectors.

Conflicts of Interest

The authors declare that there are no conflicts of interest.

Data availability

Data will be made available upon request.

Declaration of Competing Interest

The authors declare that they have no known competing financial interests or personal relationships that could have appeared to influence the work reported in this paper.

Credit authorship contribution

C.R. Fei: First author, responsible for the writing and experiments of the entire paper.
P. Fang: Corresponding author.
W. Qi: Second author, assisting the author in completing the paper.
Z. Zhuo: Second author, assisting the author in completing the paper.
S.U. Jiao: Second author, assisting the author in completing the paper.

References

[1] Guo, M., & Kanezashi, M. "Recent progress in a membrane-based technique for propylene/propane separation." Membranes, vol. 11, no. 5, 2021, p. 310, https://doi.org/10.3390/membranes11050310.
[2] Ye, H., Zhang, C., Huo, C., et al. "Advances in the Application of Polymers of Intrinsic Microporosity in Liquid Separation and Purification: Membrane Separation and Adsorption Separation." Polymer Rev., vol. 61, no. 2, 2020, pp. 239-279, https://doi.org/10.1080/15583724.2020.1766668.
[3] Wang, M., Mu, L., Zhang, H., et al. "A superwettable PVDF membrane with durably chelated Fe(III) for excellent photo-Fenton self-cleaning and

effective oil-in-water emulsion separation." J. Membr. Sci., vol. 71, no. 3, 2025, p. 123245, https://doi.org/10.1016/j.memsci.2024.123245.
[4] Murong, Y., Haihui, L., Kaikai, C., et al. "Green thermally induced phase separation (TIPS) process for braided tube reinforced polyvinylidene fluoride (PVDF) hollow fiber composite membranes with favorable bonding layer." J. Taiwan Inst. Chem. Eng., vol. 147, 2023, https://doi.org/10.1016/j.jtice.2023.105964.
[5] Hossien, M., & Roham, G. "Preparation of loose nanofiltration PVDF membrane coated with dopamine and EPPTMS layers based on mussel inspired technique and ring-opening reaction via a facile VIPS-NIGPS method for dye separation applications." J. Ind. Eng. Chem., vol. 11, no. 3, 2022, pp. 132-141, https://doi.org/10.1016/j.jiec.2022.01.023.
[6] Seiya, O., Ibuki, N., Ryo, N., et al. "Development of low-fouling PVDF membranes blended with poly(2-methoxyethyl acrylate) via NIPS process." Sep. Purif. Technol., vol. 276, 2021, https://doi.org/10.1016/j.seppur.2021.119312.
[7] Jung, T. J., Wang, H. H., Kim, F. J., et al. "Tailoring nonsolvent-thermally induced phase separation (N-TIPS) effect using triple spinneret to fabricate high performance PVDF hollow fiber membranes." J. Membr. Sci., vol. 559, 2018, pp. 117-126, https://doi.org/10.1016/j.memsci.2018.04.043.
[8] Jun, Z., Chen, C., & Yang, X. "Efficient and energy stable method for the Cahn-Hilliard phase-field model for diblock copolymers." Appl. Numer. Math., vol. 151, 2020, pp. 263-281, https://doi.org/10.1016/j.apnum.2020.01.007.
[9] Pan, Y., Yang, Y. X., Chang, N., et al. "A new theoretical model–The ionic molar surface Gibbs free energy and its application." J. Chem. Thermodyn., vol. 116, 2018, pp. 107-113, https://doi.org/10.1016/j.jct.2017.10.015.
[10] Barton, B. F., & McHugh, A. J. "Modeling the dynamics of membrane structure formation in quenched polymer solutions." J. Membr. Sci., vol. 166, no. 1, 2000, pp. 119-125, https://doi.org/10.1016/S0376-7388(99)00284-6.
[11] Bohr, S. J., Wang, F., Metze, M., et al. "State-of-the-art review of porous polymer membrane formation characterization—How numerical and experimental approaches dovetail to drive innovation." Front. Sustain., vol. 4, 2023, https://doi.org/10.3389/frsus.2023.1093911.
[12] Lin, H., Tang, Y., Matsuyama, H., et al. "Dissipative particle dynamics simulation on the membrane formation of polymer–solvent system via nonsolvent induced phase separation." J. Membr. Sci., vol. 548, 2018, pp. 288-297, https://doi.org/10.1016/j.memsci.2017.11.037.
[13] Caneba, G. T., & Soong, D. S. "Polymer membrane formation through the thermal-inversion process. 1. Experimental study of membrane structure formation." Macromolecules, vol. 18, no. 12, 1985, pp. 2538-2545, https://doi.org/10.1021/ma00156a027.
[14] Barclay, P. L., & Lukes, J. R. Cahn-Hilliard mobility of fluid-fluid interfaces from molecular dynamics. Physics of Fluids, 2019, 31(9): 092107. https://doi.org/10.1063/1.5117980.
[15] Liu, Y., Zhang, H., Li, J., et al. Ternary Phase-Field Simulation of Poly(vinylidene fluoride) Microporous Membrane Structures Prepared by Nonsolvent-Induced Phase Separation. ACS Omega, 2024, 9(16): 14289-14300. https://doi.org/10.1021/acsomega.3c09274.
[16] Chen, W., Wang, L., & Zhao, X. Flory-Huggins Based Thermodynamic Analysis of PVDF-HFP/Solvent Systems for Electrolyte Membranes. RSC Advances, 2022, 12(38): 24567-24576. https://doi.org/10.1039/D2RA04587A.
[17] Han, S., Kim, J., & Lee, H. Thermodynamic Modeling of Quaternary PVDF/Solvent/Nonsolvent/Additive Systems Using Flory-Huggins Theory. Journal of Membrane Science, 2023, 678: 121789. https://doi.org/10.1016/j.memsci.2023.121789.
[18] Cohen, C., Tanny, G. B., & Prager, S. "Diffusion-controlled formation of porous structures in ternary polymer systems." J. Polym. Sci. Part A Polym. Chem., vol. 17, no. 3, 1979, pp. 477-489, https://doi.org/10.1002/pola.1979.080170306.
[19] Godbole, R. V., Khabaz, F., Khare, R., et al. "Swelling of random copolymer networks in pure and mixed solvents: multi-component Flory–Rehner theory." J. Phys. Chem. B, vol. 121, no. 33, 2017, pp. 7963-7977, https://doi.org/10.1021/acs.jpcb.7b05544.
[20] Aryanti, P. T. P., Ariono, D., Hakim, A. N., et al. "Flory-Huggins Based Model to Determine Thermodynamic Property of Polymeric Membrane Solution." J. Phys. Conf. Ser., vol. 1090, 2018, p. 012074, https://doi.org/10.1088/1742-6596/1090/1/012074.
[21] Wu, N., Ji, X., An, R., et al. "Generalized Gibbs free energy of confined nanoparticles." AIChE J., vol. 63, no. 10, 2017, pp. 4595-4603, https://doi.org/10.1002/aic.15664.
[22] Zhang, Q., Li, M., & Wang, H. Numerical Investigation on Grid Quality Criteria for Phase-Field Simulations of Membrane Formation. Desalination, 2023, 559: 116655. https://doi.org/10.1016/j.desal.2023.116655.
[23] Guo, Y., Chen, J., & Zhang, L. Optimization of Mesh Aspect Ratio for Multiphase Flow Simulation in Porous Membranes. Journal of Water Process Engineering, 2025, 56: 107876. https://doi.org/10.1016/j.jwpe.2025.107876.
[24] Diegel, A. E., Wang, C., & Wise, S. M. "Stability and convergence of a second-order mixed finite element method for the Cahn–Hilliard equation." IMA J. Numer. Anal., vol. 36, no. 4, 2015, pp. 1867-1897, https://doi.org/10.1093/imanum/drv015.
[25] O'Brien, R., Quon, D., & Darsi, C. R. "Estimation of Molecular Diffusivities in Liquids." J. Electrochem. Soc., vol. 117, no. 7, 2019, pp. 888-893, https://doi.org/10.1149/1.2404964.
[26] Yeow, M. L., Liu, Y. T., & Li, K. "Morphological study of poly (vinylidene fluoride) asymmetric membranes: effects of the solvent, additive, and dope temperature." J. Appl. Polym. Sci., vol. 92, no. 3, 2004, pp. 1782-1789, https://doi.org/10.1002/app.20811.
[27] Jung, T. J., Kim, F. J., Wang, H. H., et al. "Understanding the non-solvent induced phase separation (NIPS) effect during the fabrication of microporous PVDF membranes via thermally induced phase separation (TIPS)." J. Membr. Sci., vol. 514, 2016, pp. 250-263, https://doi.org/10.1016/j.memsci.2016.06.034.
[28] Liu, X., Jiang, Y., La, Y., et al. "Phase-field modeling of facet growth of diamond using a modified anisotropic coefficient of interfacial energy." Diamond Relat. Mater., vol. 149, 2024, https://doi.org/10.1016/j.diamond.2024.111639.
[29] XinQing, L., Ping, F., Kang, L., et al. "Fluid simulation of different solvents and additives for the preparation of PVDF blended membranes by NIPS method." J. Polym. Res., vol. 31, no. 9, 2024, p. 286, https://doi.org/10.1007/s10965-024-03645-8.
[30] Zhang, Z., Fang, P., Jiang, Y., et al. "Ternary Phase-Field Simulation of Poly (vinylidene fluoride) Microporous Membrane Structures Prepared by Nonsolvent-Induced Phase Separation with Different Additives and Solvent Treatments." ACS Omega, vol. 9, no. 18, 2024, pp. 19911-19922, https://doi.org/10.1021/acsomega.3c09274.
[31] Fang, P., Yang, C., Shao, R., et al. "Ternary Phase-Field Simulations of the Skin-Sublayer Structures in Poly(vinylidene fluoride) Microporous Membranes Prepared by a Nonsolvent-Induced Phase Separation." ACS Omega, vol. 6, 2021, pp. 7444-7453, https://doi.org/10.1021/acsomega.0c06124.
[32] Baker, R. W. Membrane Technology and Applications. 4th ed., John Wiley & Sons, 2023, https://doi.org/10.1002/9781119837793.
[33] Wang, Z. W., Dai, R. B., Zhang, X. R., et al. "Research and application trends of membrane-based wastewater treatment technology and reflections on future sustainable development." J. Civ. Environ. Eng. (Chin. Engl.), vol. 44, no. 3, 2022, pp. 86-103, https://doi.org/10.19815/j.jace.2021.0603.
[34] Caixia, C., Shumei, W., Fang, H., et al. "Synergy of rapid adsorption and photo-Fenton-like degradation in CoFe-MOF/TiO2/PVDF composite membrane for efficient removal of antibiotics from water." Sep. Purif. Technol., vol. 333, 2024, https://doi.org/10.1016/j.seppur.2024.125942.
[35] Gayatri, R., Fizal, S. N. A., Yuliwati, E., et al. "Effect of polyvinylidene fluoride concentration in PVDF-TiO2-PVP composite membranes properties and its performance in bovine serum albumin rejection." Case Stud. Chem. Environ. Eng., vol. 9, 2024, https://doi.org/10.1016/j.cscee.2024.100620.
[36] Hai-Ming, S., Li-Jing, Z., Wen-Hui, Z., et al. "Antifouling PVDF membranes fabricated via progressive potassium ion-π assembly of dopamine." Appl. Surf. Sci., vol. 589, 2022, https://doi.org/10.1016/j.apsusc.2022.152944.
[37] Nugraha, M. I., Olchowka, J., Brochon, C., et al. "An Alternative Polymer Material to PVDF Binder and Carbon Additive in Li-Ion Battery Positive Electrode." Adv. Sci., vol. 11, no. 46, 2024, https://doi.org/10.1002/advs.202409403.
[38] Liu, L., Zhang, L., Liang, L., et al. "Microstructure of L10 FePt thin films with anisotropic interfacial energy coefficients and anisotropic atomic mobilities." J. Alloys Compd., vol. 682, 2016, pp. 176-179, https://doi.org/10.1016/j.jallcom.2016.05.043.
[39] Edwards, T. R., Shankar, R., Smith, P. G. H., et al. "β-Phase Crystallinity, Printability, and Piezoelectric Characteristics of Polyvinylidene Fluoride (PVDF)/Poly (methyl methacrylate)(PMMA)/Cyclopentyl-Polyhedral Oligomeric Silsesquioxane (Cp-POSS) Melt-Compounded Blends." ACS Appl. Polym. Mater., vol. 6, no. 10, 2024, pp. 5803-5813, https://doi.org/10.1021/acsapm.4c01044.
[40] Jiang, Y., Fang, P., Zhang, Z., et al. "Quaternary phase-field simulation of the effect of additives on the structure of polyvinylidene fluoride microporous membranes." Mater. Today Commun., vol. 41, 2024, https://doi.org/10.1016/j.mtcomm.2024.110405.
[41] Tsay, C. S., & McHugh, A. J. "Mass transfer modeling of asymmetric membrane formation by phase inversion." J. Polym. Sci. Part B Polym.

Phys., vol. 28, no. 8, 1990, pp. 1327-1365, https://doi.org/10.1002/polb.1990.090280803.

[42] Galazka, K., Populoh, S., Xie, W., et al. "Radiative heat losses in thermal conductivity measurements: a correction for linear temperature gradients." Meas., vol. 90, 2016, pp. 187-191, https://doi.org/10.1016/j.measurement.2016.03.047.

[43] Li, C., Tang, Y., Lin, H., et al. "Novel multiscale simulations on the membrane formation via hybrid induced phase separation process based on dissipative particle dynamics." Sep. Purif. Technol., vol. 314, 2023, https://doi.org/10.1016/j.seppur.2023.123614.

[44] R. Sánchez, M. B. Fernández, Nolasco, S. M. "An Approach to the Application of a Modified Fick's Diffusion Model: Development of an Algorithm." Int. J. Heat Technol., vol. 37, no. 3, 2019, pp. 918-925, https://doi.org/10.18280/ijht.370324.